PROCEEDINGS OF THE ROYAL SOCIETY A

rspa.royalsocietypublishing.org

Research

Cite this article: Xue Y, Yuan H, Su W, Shi Y, Duan H. 2014 Enhanced load-carrying capacity of hairy surfaces floating on water. *Proc. R. Soc. A* **470**: 20130832.
http://dx.doi.org/10.1098/rspa.2013.0832

Received: 16 December 2013
Accepted: 7 February 2014

Subject Areas:
mechanical engineering, fluid mechanics, mathematical modelling

Keywords:
hairy surfaces, superhydrophobicity, free energy analysis, load-carrying capacity

Author for correspondence:
Huiling Duan
e-mail: hlduan@pku.edu.cn
Yipeng Shi
e-mail: syp@mech.pku.edu.cn

Enhanced load-carrying capacity of hairy surfaces floating on water

Yahui Xue[1], Huijing Yuan[1], Weidong Su[1], Yipeng Shi[1] and Huiling Duan[1,2]

[1]State Key Laboratory for Turbulence and Complex Systems, Department of Mechanics and Engineering Science, College of Engineering, and [2]Key Laboratory of High Energy Density Physics Simulation (HEDPS), CAPT, Peking University, Beijing 100871, People's Republic of China

Water repellency of hairy surfaces depends on the geometric arrangement of these hairs and enables different applications in both nature and engineering. We investigate the mechanism and optimization of a hairy surface floating on water to obtain its maximum load-carrying capacity by the free energy and force analyses. It is demonstrated that there is an optimum cylinder spacing, as a result of the compromise between the vertical capillary force and the gravity, so that the hairy surface has both high load-carrying capacity and mechanical stability. Our analysis makes it clear that the setae on water striders' legs or some insects' wings are in such an optimized geometry. Moreover, it is shown that surface hydrophobicity can further increase the capacity of a hairy surface with thick cylinders, while the influence is negligible when the cylinders are thin.

1. Introduction

Superior water-repellency of hydrophobic rough/hairy surfaces can be used for applications of lowering the adhesive force of water droplets on solid surfaces, reducing drag for microfluidic devices and marine vessels and so on [1,2]. Valuable inspirations for designing such surfaces have been provided by nature [3–7]. For example, the lotus leaf with two-level hierarchical pillar structures exhibits ultra-low adhesive force to water [8]. Water striders can move effortlessly on water because of the special setae structures on their legs [9,10]. Hairy layers on the surfaces of the legs and wings

Royal Society Publishing

help some flying insects living in a humid environment to avoid being wetted by rain and other water surfaces they may encounter [11,12]. Some insects and fish spiders living in marine habitats are able to stay underwater for a long time with a thin layer of air along their hairy body surface, which enables their respiration underwater [13–15]. Research interest has been paid to achieve high load-carrying capacity of porous/hairy surfaces by rendering them superhydrophobic as inspired by nature. Marmur & Ras [16] pointed out that the load-carrying capacity of porous rafts can be improved by the micro/nano-scaled inner pores at the raft bottoms. Miniature boats fabricated from copper meshes rendered superhydrophobic have shown remarkable loading capacity [17,18]. Hydrophobic powders enable liquid marbles to float on water surfaces [19]. Superhydrophobic carbon fibre fabrics and nanocellulose aerogel membranes have also proved to be good cargo-carriers on water, even on oil for the latter [20,21].

Water-repellent properties of rough surfaces with pillars or pores have been much investigated. Special attention is being paid to the water-repellent property of surface structures made from thin hairs or fibres [22,23]. Schematics of a water strider's leg and a fly's wing covered by setae/hairs are shown in figure 1*a*,*b*, respectively. The setae/hairs provide resistance for the surface to getting wetted by water. Many researchers have tried to understand how the hairy structures render legs or wings of some insects water repellent from the point of view of surface physics and chemistry. Gao & Jiang [9] have carried out sessile water-drop measurements and shown that the water strider's legs are superhydrophobic (i.e. the wetting contact angle of water droplet approx. 168°). Experiments have found that the wings of the cranefly also exhibit superhydrophobicity [12]. It is pointed out that the superhydrophobicity of water striders' legs is due to the conjunction of the nano-grooved oriented setae and the wax on the leg surface [24]. While theoretical calculations [25,26] have shown that the maximum buoyant force of a thin rod does not change much with the increase in the surface hydrophobicity, Lee & Kim [27] and Su *et al.* [28] have clarified that superhydrophobicity plays more important roles in lowering the adhesion and energy dissipation during the locomotion of water striders on water. Moreover, it is argued that the flexibility of the water striders' legs also contributes to their super water-repellency [29–31].

In general, the existing studies are mainly focused on the apparent effects of hairy structures on surface hydrophobicity, floating or adhesion property. In fact, water-repellency of hairy surfaces depends on the size, spacing and orientation of the hairs [32,33]. When those hairs/setae are brought into contact with water, a large number of micro-menisci are formed, which render insects' legs or wings water repellent for particular functions (e.g. maximum load-carrying capacity, low adhesion, drag reduction, plastron respiration, etc.). The morphology of the menisci depends on the interaction between nearby hairs. The supporting force given by these menisci resists the penetration of water [13–15]. To keep the water-repellency, the spacing between those hairs should be small so that the liquid–air interfaces can stand the highest impact they may experience in their living environment, according to the Young–Laplace equation. On the other hand, densely packed hairs near the surface decrease the area fraction of the air–water interface, which hinders hairy surfaces in their particular functions. Therefore, a structural optimization of those hairy surfaces is needed. For example, the higher the supporting force can be provided by those hairs per unit area, the smaller part of a water striders' leg or a fly's wing will be wetted during a stroke on water or impact by a droplet (figure 1*a*,*b*). However, to the best of authors' knowledge, till now the mechanism of the hair interaction and the influence on the water-repellency have hardly been discussed, nor has the optimization design of a hairy surface to achieve the maximum supporting force per unit area.

In this paper, by adapting a simplified model of a hairy surface made from parallel cylinders floating on water, we investigate the mechanism and optimization of its water-repellency by applying both free energy and force analyses, with the aim to achieve the maximum load-carrying capacity and mechanical stability. This paper is organized as follows. In §2, we describe the variation of the meniscus shape when quasi-statically changing the vertical position of the hairy surface. In §3, we calculate the free energy change with respect to a reference state. The applied force needed to balance the cylinders is derived by differentiating the total free energy change

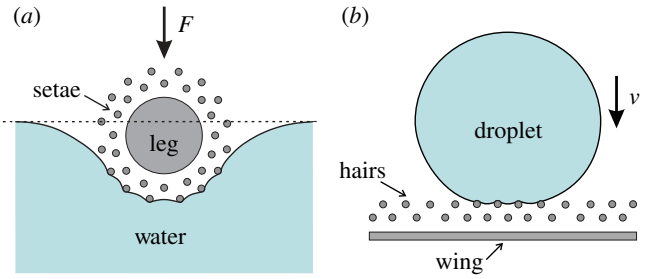

Figure 1. Schematics of the cross sections of (*a*) a water strider's leg surrounded by uniformly distributed setae and pressed against water by a load *F*, and (*b*) a fly's wing with hairs impacted by a droplet with a velocity v. (Online version in colour.)

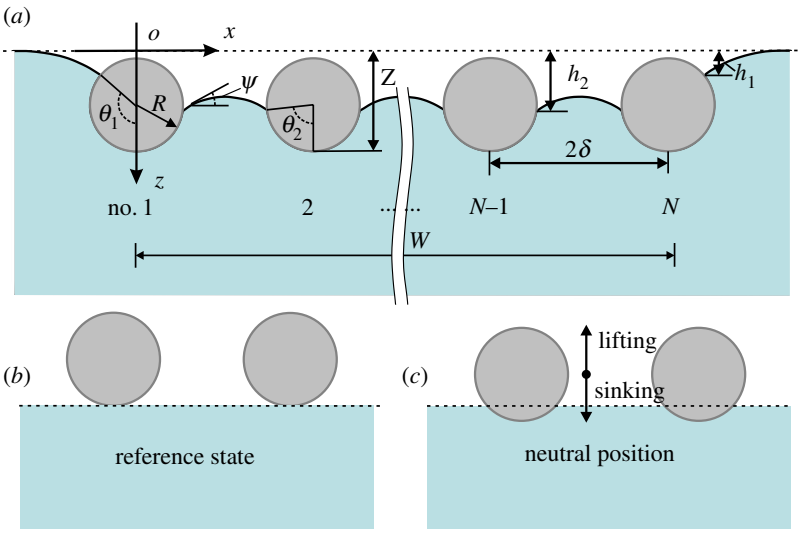

Figure 2. Schematic of a hairy surface made of *N* thin parallel cylinders floating on water under load: (*a*) current state, (*b*) reference state and (*c*) neutral position. (Online version in colour.)

with respect to the displacement. Respective free energy and force contributions by the inside and outside cylinders are compared. In §4, for a hairy surface of a given size, we investigate its optimization design to obtain the maximum load capacity and mechanical stability. In §5, concluding remarks are given.

2. Meniscus shapes

The buoyant force of an object floating on water is usually estimated by Archimedes' principle. When the size of the object is comparable to or much smaller than the capillary length a ($=\sqrt{\gamma/\rho g}$, where γ is surface tension, ρ density and g gravity acceleration), the effect of surface tension needs to be considered [34]. Although the hairs on water striders' legs are circularly distributed (figure 1*a*), for brevity but without losing the main physical picture, we consider a simple two-dimensional model in which a hairy surface made from *N* thin cylinders lying straightly parallel to each other is pressed against water, as shown in figure 2. Those cylinders are assumed to be rigid and hydrophobic.

A possible equilibrium state of the hairy surface under load is shown in figure 2*a*, in which the menisci formed along the boundary and inside cylinders protrude upward to resist sinking.

The equilibrium state is available when the load is smaller than the load-carrying capacity of the hairy surface. The radius, length and spacing of those cylinders are denoted by R, L and 2δ, respectively. The width of the hairy surface is W (figure 2*a*). We assume $L \gg R$ so that a three-dimensional effect of the menisci is negligible. Here, θ_Y is the Young contact angle, and θ_1 and θ_2 denote the half sector angles of the wetted outside and inside cylinders, respectively. Here and in the following, subscripts 1 and 2 refer to the outside and inside menisci/cylinders, respectively. We use Z to denote the displacement of the cylinders, and h_i ($i = 1, 2$) the position of the menisci with respect to a reference state, as shown in figure 2*b*, that is, the stationary state just before the bottom of the cylinders touches the water surface. We define a neutral position, where the menisci along the cylinders are horizontal (as shown in figure 2*c*).

Under the Cartesian coordinate system (o–xz) as shown in figure 2*a*, the balance between the Laplace pressure difference and the gravity potential gives the governing equations of the meniscus [35]:

$$\frac{\mathrm{d}}{\mathrm{d}x}\sin\psi = -a^{-2}z \quad \text{and} \quad \frac{\mathrm{d}z}{\mathrm{d}x} = -\tan\psi. \tag{2.1}$$

Here, ψ is introduced as a geometric parameter. To present a general analysis, we introduce non-dimensional parameters

$$\tilde{x} = \frac{x}{a}, \quad \tilde{z} = \frac{z}{a}, \quad \tilde{L} = \frac{L}{a}, \quad \tilde{W} = \frac{W}{a}, \quad \tilde{\delta} = \frac{\delta}{a}, \quad \tilde{Z} = \frac{Z}{a} \quad \text{and} \quad \mathrm{Bo} = \left(\frac{R}{a}\right)^2, \tag{2.2}$$

where Bo is the Bond number [27]. With boundary conditions $\tilde{z} = \tilde{h}_2 = \eta\sqrt{2}\sqrt{c_2 + \cos(\theta_Y + \theta_2)}$, $\tilde{x} = \sqrt{\mathrm{Bo}}\sin\theta_2$ at the contact line, i.e. $\psi = \psi_2$ (where $\psi_i = \theta_i + \theta_Y - \pi$, $i = 1$ and 2) and $\tilde{x} = \tilde{\delta}$ at $\psi = 0$, we derive the expression for the inside meniscus

$$\left.\begin{aligned} &\tilde{z}(\psi) = \eta\sqrt{2}\sqrt{c_2 - \cos\psi} \\ \text{and} \quad &\tilde{x}(\psi) = \eta\frac{\sqrt{2}}{\sqrt{c_2 - 1}}\left[(c_2 - 1)\mathbf{EE}\left(\frac{\psi}{2}, \frac{2}{1 - c_2}\right) - c_2\mathbf{EF}\left(\frac{\psi}{2}, \frac{2}{1 - c_2}\right)\right] + \tilde{\delta}, \end{aligned}\right\} \tag{2.3}$$

where $\mathbf{EF}(\phi, m) = \int_0^\phi (1 - m\sin^2\theta)^{-1/2}\mathrm{d}\theta$ and $\mathbf{EE}(\phi, m) = \int_0^\phi (1 - m\sin^2\theta)^{1/2}\mathrm{d}\theta$, representing the incomplete elliptic integrals of the first and the second kinds, respectively. At the neutral position, we have $\psi_i = 0$, i.e. $\theta_i = \pi - \theta_Y$ ($i = 1$, 2). In equation (2.3), η is equal to 1 or -1. Here, $\eta = 1$ represents the state of sinking, that is, the cylinders are pressed against water and the menisci protrude upward, i.e. $\psi_i > 0$. On the other hand, $\eta = -1$ represents the state of lifting, that is, the cylinders are lifted up from water and the menisci sag downward, i.e. $\psi_i < 0$ (figure 2*c*). Note that $\tilde{h}_2$ is related to $\tilde{h}_1$ by $\tilde{Z}$, that is,

$$\tilde{h}_2 + \sqrt{\mathrm{Bo}}(1 - \cos\theta_2) = \tilde{h}_1 + \sqrt{\mathrm{Bo}}(1 - \cos\theta_1) = \tilde{Z}. \tag{2.4}$$

The parameter c_2 is determined by

$$\eta\frac{\sqrt{2}}{\sqrt{c_2 - 1}}\left[(c_2 - 1)\cdot\mathbf{EE}\left(\frac{\psi_2}{2}, \frac{2}{1 - c_2}\right) - c_2\cdot\mathbf{EF}\left(\frac{\psi_2}{2}, \frac{2}{1 - c_2}\right)\right] + \tilde{\delta} = \sqrt{\mathrm{Bo}}\sin\theta_2. \tag{2.5}$$

For a given hairy surface, equation (2.4) expresses the dependence of θ_2 on $\tilde{Z}$ or θ_1. When combined with equation (2.4), equation (2.5) can be easily solved numerically to get θ_2 and c_2 for a given displacement $\tilde{Z}$ of the raft. Then, the profile of the inside meniscus can be investigated based on equation (2.3).

With the assumption of small spacing between cylinders (i.e. $\tilde{\delta} \ll 1$), or small curvature variation along the meniscus, the expression for the inside meniscus (i.e. equation (2.3)) can be

reduced and simply given by the Laplace equation that neglects the effects of gravity [13,15,16,36], that is,

$$\Delta P = \frac{\gamma}{r}, \tag{2.6}$$

where ΔP ($= \rho g h_2$) is the Laplace pressure difference across the meniscus and r is the constant curvature radius of the meniscus

$$r = \frac{\delta - R\sin\theta_2}{\sin\psi_2}. \tag{2.7}$$

In the case of a small spacing, r and ψ_2 determine the shape and position of the inside meniscus and can be resolved by equations (2.6) and (2.7).

When the spacing between nearby cylinders is much larger than the capillary length, i.e. $\tilde{\delta} \gg 1$, the interaction between nearby cylinders becomes very weak and the inside and outside menisci exhibit a similar profile. Thus, the expression for the outside menisci can be obtained by equation (2.3) with $\tilde{\delta} \to \infty$, which leads to

$$\tilde{x} = \ln\left(\frac{2+\sqrt{2-\tilde{z}^2}}{\eta\tilde{z}}\right) - \sqrt{4-\tilde{z}^2} + c_1, \tag{2.8}$$

where

$$c_1 = \sqrt{\mathrm{Bo}}\sin\theta_1 - \ln\left(\frac{2+\sqrt{2-\tilde{h}_1^2}}{\eta\tilde{h}_1}\right) + \sqrt{4-\tilde{h}_1^2}, \tag{2.9}$$

and $\tilde{h}_1 = \eta\sqrt{2}\sqrt{1-\cos\psi_1}$. The analytical solution (2.8) has been obtained by Liu *et al.* [26]. The shape of the outside meniscus has been well investigated [26,35]. In the following, we focus on how the hair interaction influences the profile of the inside meniscus.

For most biological materials covered with smooth wax, θ_Y has a value approximately 105° [9]. The Bond number of water striders' legs is approximately 1×10^{-3} and that of the setae on those legs is approximately 1×10^{-7} [9,37]. Here, we use an intermediate value of $\mathrm{Bo} = 1 \times 10^{-4}$ and $\theta_Y = 105°$ to illustrate the variation of the profile of the inside meniscus when the position of the raft is quasi-statically changed. Plots of θ_2 as a function of $\tilde{\delta}$ with respect to different θ_1 are shown in figure 3. According to equation (2.4), θ_1 uniquely represents the position of the raft: sinking when $\theta_1 > 75°$ and lifting when $\theta_1 < 75°$. For the chosen values of θ_1, the variation of θ_2 shows a similar trend with the increase of $\tilde{\delta}$: initially slight change around the neutral position (i.e. $\theta_2 = 75°$) when $\tilde{\delta} < 0.1$ and then dramatic change until approaching a value close to θ_1 when $\tilde{\delta} > 0.1$. A value of θ_2 close to θ_1 means that the interaction between the nearby cylinders becomes weak. At $\tilde{\delta} = 0.1$, we plot the profiles of the inside menisci for different positions during the sinking (e.g. $\theta_1 = 100°$, 130° and 160°) and lifting (e.g. $\theta_1 = 60°$, 30° and 0°) processes in figure 4. When sinking, the inside meniscus protrudes upward to balance the increased hydrostatic pressure; when lifting, the meniscus sags downward to resist lifting. With the profiles of the outside and inside menisci known, we will investigate the free energy and buoyant force of a hairy surface floating on water in §3.

3. Free energy and buoyant force

The method of free energy analysis has been widely used to study the wetting phenomenon of liquid on solid surfaces [38–41]. For example, Rapacchiettta *et al.* [38] applied free energy analysis to study the interaction between a single cylinder and water surface. They compared the energy method with the force analysis method and demonstrated that the former is more comprehensive in displaying subtle characteristics of the systems. Lee & Kim [26] proposed a criterion for lifting a cylinder from water based on free energy analysis. Su *et al.* [28] calculated the energy dissipation of a cylinder by integrating the buoyant force with respect to the displacement. In this section, based on the meniscus profiles calculated in §2, we will calculate the free energy change of the system when quasi-statically changing the mechanically enforced stationary positions of the hairy

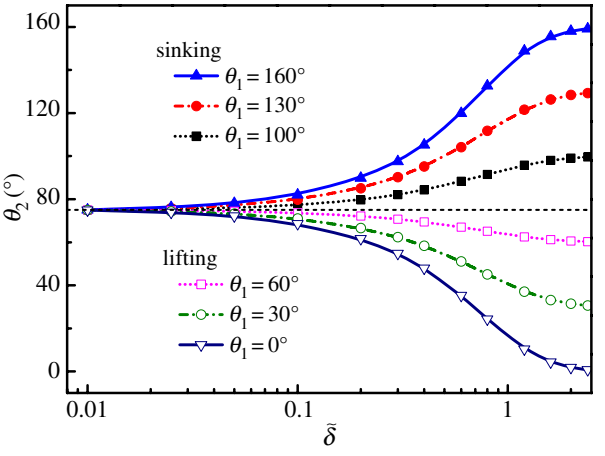

Figure 3. Plots of θ_2 as a function of $\tilde{\delta}$ with respect to different θ_1 for Bo $= 1 \times 10^{-4}$ and $\theta_Y = 105°$. Sinking positions: $\theta_1 =$ 100°, 130° and 160° and lifting positions: $\theta_1 = 60°$, 30° and 0°. The black dashed line shows the neutral position (i.e. $\theta_2 =$ 75°). (Online version in colour.)

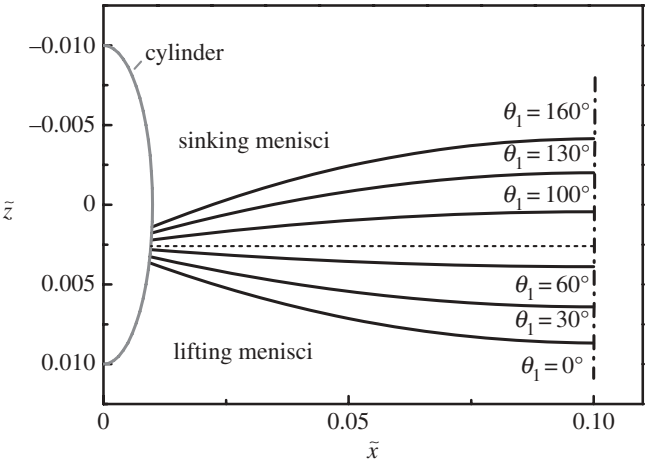

Figure 4. The profiles of the inside menisci at different positions: sinking ($\theta_1 = 100°$, 130° and 160°) and lifting ($\theta_1 = 60°$, 30° and 0°) for Bo $= 1 \times 10^{-4}$, $\tilde{\delta} = 0.1$ and $\theta_Y = 105°$.

surface, with respect to a reference state as shown in figure 2*b*. The free energy change is the energy barrier that the load needs to conquer before the surface reaches a certain position, or the negative work done by the buoyant force. A higher free energy change represents higher mechanical stability. Therefore, the buoyant force can be derived by differentiating the free energy change with respect to the displacement.

The total free energy of the system includes two parts: the surface free energy and gravitational potential energy. The energy E is non-dimensionalized by $aL\gamma$, i.e. $\tilde{E} = E/(aL\gamma)$. The surface free energy associated with the outside menisci is expressed as

$$\tilde{E}_{S1} = -2\sqrt{\text{Bo}}(\theta_1 \cos\theta_Y + \sin\theta_1) + 4 - 2\sqrt{2}\sqrt{1 + \cos\psi_1}. \tag{3.1}$$

The surface free energy associated with each inside meniscus is expressed as

$$\tilde{E}_{S2} = -2\sqrt{\mathrm{Bo}}\theta_2 \cos\theta_Y - 2\tilde{\delta} + \eta \frac{2\sqrt{2}}{\sqrt{c_2 - 1}} \mathbf{EF}\left(\frac{\psi_2}{2}, \frac{2}{1 - c_2}\right). \tag{3.2}$$

The changes of the gravitational potential energy per cylinder, and the outside and inside menisci are denoted by $\tilde{E}_{Gs}$, $\tilde{E}_{G1}$ and $\tilde{E}_{G2}$, respectively,

$$\tilde{E}_{Gs} = -\pi \mathrm{Bo} De \tilde{Z}, \tag{3.3}$$

$$\tilde{E}_{G1} = \mathrm{Bo}^{3/2}\left[-\theta_1 \cos\theta_1 - \frac{\tilde{h}_1}{\sqrt{\mathrm{Bo}}}(-\theta_1 + \sin\theta_1 \cos\theta_1) + \sin\theta_1 - \frac{1}{3}\sin^3\theta_1\right] + \frac{1}{3}(\sqrt{4 - \tilde{h}_1^2} + 3\tilde{h}_1^2\sqrt{\mathrm{Bo}}\sin\theta_1 - 4) \tag{3.4}$$

and

$$\tilde{E}_{G2} = \mathrm{Bo}^{3/2}\left[-\theta_2 \cos\theta_2 - \frac{\tilde{h}_2}{\sqrt{\mathrm{Bo}}}(-\theta_2 + \sin\theta_2 \cos\theta_2) + \sin\theta_2 - \frac{1}{3}\sin^3\theta_2\right] + \frac{2\sqrt{2}\eta}{3}\sqrt{c_2 - 1}\left[(c_2 + 1) \cdot \mathbf{EF}\left(\frac{\psi_2}{2}, \frac{2}{1 - c_2}\right) - c_2 \cdot \mathbf{EE}\left(\frac{\psi_2}{2}, \frac{2}{1 - c_2}\right)\right] + \frac{2\sqrt{2}\eta}{3}\sqrt{c_2 - \cos\psi_2}\sin\psi_2 + \sqrt{\mathrm{Bo}}\sin\theta_2\tilde{h}_2^2, \tag{3.5}$$

where De is the ratio of the cylinder density ρ_s and the water density ρ_l. When the Bond number is small (e.g. $\mathrm{Bo} < 0.01$), the effect of cylinder's gravity is negligible. We choose $De = 1.2$, which corresponds to the density of most biomaterials. Note that all the inside menisci are the same. The total free energy change of a hairy surface is given by

$$\tilde{E} = \tilde{E}_1 + (N - 1)\tilde{E}_2, \tag{3.6}$$

where $\tilde{E}_1$ $(= \tilde{E}_{S1} + \tilde{E}_{G1} + \tilde{E}_{Gs})$ and $\tilde{E}_2$ $(= \tilde{E}_{S2} + \tilde{E}_{G2} + \tilde{E}_{Gs})$ are the free energies contributed by each outside and inside cylinders, respectively.

Figure 5 illustrates the diagrams of the free energy changes $\tilde{E}_1$ and $\tilde{E}_2$ at different stationary positions represented by θ_1. Similar behaviour is found for both $\tilde{E}_1$ and $\tilde{E}_2$. At the neutral position, the free energy change is the lowest. Both the sinking and lifting of those cylinders increase the free energy change. The free energy difference with respect to the neutral position denoted by $\Delta\tilde{E}$ $(= \tilde{E} - \tilde{E}_{n.p.}$, where $\tilde{E}_{n.p.}$ is the free energy at the neutral position as shown in figure 2*c*) is the energy needed to sink or lift those cylinders to a certain position with respect to the neutral one. From figure 5, we can see that, as the surface hydrophobicity increases, while the sinking energy increases slightly, the lifting energy decays more pronouncedly. This means that a superhydrophonic cylinder can be lifted up from water much easier than a normally hydrophobic one. Our finding here is consistent with known concepts about the roles of surface hydrophobicity on the floating of a single cylinder on water [25–28].

For a given hairy surface, the total sinking or lifting energy needed to put it at a certain position is equal to the negative work done by the buoyant force. With equations (2.4) and (3.6), we have

$$\tilde{F}_i = \frac{\partial \Delta\tilde{E}_i}{\partial \tilde{Z}} = \frac{\partial \Delta\tilde{E}_i}{\partial \theta_i} \Big/ \frac{\partial \tilde{Z}}{\partial \theta_i}. \tag{3.7}$$

Combination of equations (3.1)–(3.5) and (3.7) yields

$$\tilde{F}_i = \mathrm{Bo}\left[\theta_i - \sin\theta_i \cos\theta_i - \frac{2}{\mathrm{Bo}}\sin(\theta_i + \theta_Y) + 2\frac{\tilde{h}_i}{\sqrt{\mathrm{Bo}}}\sin\theta_i - \pi De\right], \tag{3.8}$$

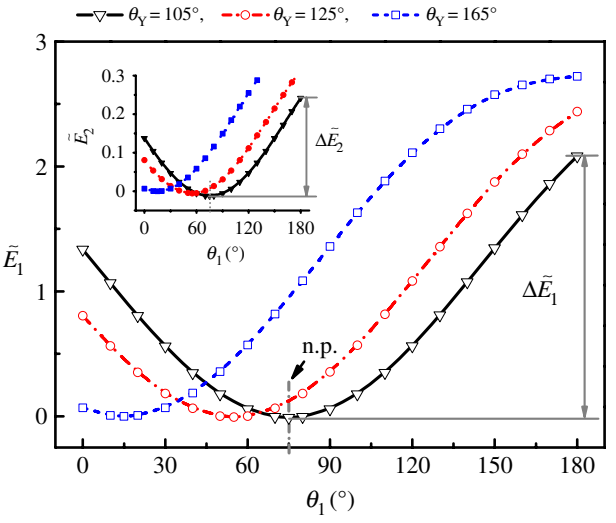

Figure 5. Diagram of the free energy change $\tilde{E}_1$ at different stationary states for $\mathrm{Bo} = 1 \times 10^{-4}$, $\tilde{\delta} = 0.1$ and different θ_Y. The inset is the diagram of $\tilde{E}_2$. The neutral position is denoted by 'n. p.', and $\Delta\tilde{E}_1$ and $\Delta\tilde{E}_2$ are the free energy differences of the outside and inside menisci with respect to the neutral position, respectively. (Online version in colour.)

which is consistent with the results obtained from direct force analysis [16,25,26]. The detailed procedure to obtain equation (3.8) can be found in appendix A. Then, the total buoyant force is given by

$$\tilde{F} = \tilde{F}_1 + (N-1)\tilde{F}_2. \tag{3.9}$$

It is interesting to see how the inside menisci contribute to the total free energy change and buoyant force during a sinking or lifting process of a hairy surface. This analysis in the following will be focused on the sinking process and the analysis of the lifting process can be obtained by following a similar procedure. During sinking, there is a position where the buoyant force generated by the outside menisci has a maximum value, i.e. $\tilde{F}_{1,\max}$, which can be obtained by letting $\partial\tilde{F}_1/\partial\theta_1 = 0$ according to equation (3.8). This maximum value corresponds to the load-carrying capacity of the outside menisci. When the outside meniscus reaches the maximum load-carrying position, the inside meniscus is still quite stable, that is, the pressure difference across the meniscus is still much smaller than the maximum Laplace pressure that can be provided (i.e. equation (2.6)). As shown in figure 3, θ_2 only approaches θ_1 in the case of $\tilde{\delta} \gg 1$. Thus, it is reasonable to assume that the submersion of the whole hairy surface is generally induced by the collapse of the outside menisci. Therefore, we refer to the maximum load-carrying position of the outside cylinders as the maximum load-carrying position of the whole hairy surface, and the load-carrying capacity $\tilde{F}_{\mathrm{cpc}}$ is a sum of $\tilde{F}_{1,\max}$ and corresponding $\tilde{F}_2$ at this position, that is,

$$\tilde{F}_{\mathrm{cpc}} = \tilde{F}_{1,\max} + (N-1)\tilde{F}_2. \tag{3.10}$$

For $\mathrm{Bo} = 1 \times 10^{-4}$ and $\theta_Y = 105^\circ$, the maximum value of $\tilde{F}_1$ is obtained at $\theta_1 \sim 165^\circ$. At this maximum load-carrying position, variations of $\Delta\tilde{E}_2$ and $\tilde{F}_2$ with $\tilde{\delta}$ are plotted in figure 6*a*,*b*, respectively. The values of $\Delta\tilde{E}_1$ and $\tilde{F}_1$ are also included for comparison. It is seen that both $\Delta\tilde{E}_2$ and $\tilde{F}_2$ increase with $\tilde{\delta}$, and especially that the behaviours of both $\Delta\tilde{E}_2$ and $\tilde{F}_2$ are approximately linear for small $\tilde{\delta}$. When $\tilde{\delta}$ is small (e.g. $\tilde{\delta} < 0.1$), $\Delta\tilde{E}_1$ and $\tilde{F}_1$ are one or even two orders of magnitude higher than $\Delta\tilde{E}_2$ and $\tilde{F}_2$, respectively. When $\tilde{\delta}$ is comparable with or even higher than 1, the interaction between the nearby cylinders becomes very weak and the contributions from the inside and outside cylinders are comparable. When $\tilde{\delta} < 0.1$, though the free energy and buoyant force contributions from each inside meniscus is much smaller than that of each outside

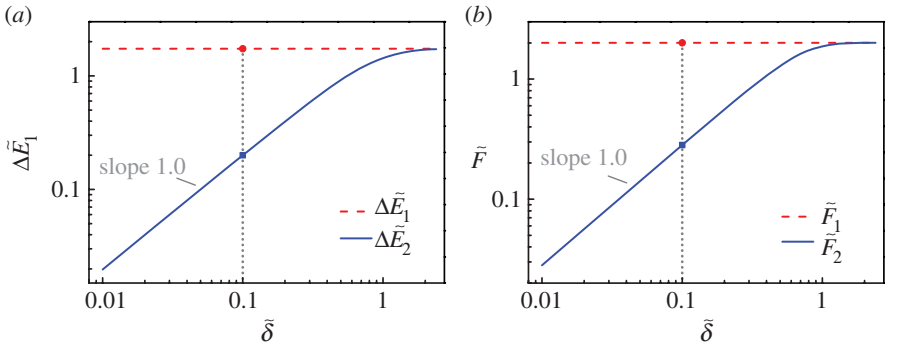

Figure 6. Variations of $\Delta\tilde{E}_2$ (*a*) and $\tilde{F}_2$ (*b*) versus $\tilde{\delta}$ and respective comparisons with $\Delta\tilde{E}_1$ and $\tilde{F}_1$ (Bo $= 1 \times 10^{-4}$ and $\theta_Y = 105^\circ$). The dotted lines show the positions of $\tilde{\delta} = 0.1$. (Online version in colour.)

meniscus, it can improve the total contribution of the inside menisci by increasing the cylinder numbers. For example, at $\tilde{\delta} = 0.1$, the values of $\Delta\tilde{E}_2$ and $\tilde{F}_2$ are 0.20 and 0.28, respectively, and the values of $\Delta\tilde{E}_1$ and $\tilde{F}_1$ are 1.73 and 2.01, respectively. With the number of the inside cylinder increased to 10, the contribution of the insider cylinders is already higher than that of the outside cylinder.

From the above analysis, it is shown that there are two ways to enhance the load-carrying capacity of a hairy surface: one by increasing the spacing between the cylinders of a constant number, as seen in figure 6, and the other by increasing the cylinder numbers while the cylinder spacing is kept constant. The former increases the vertical capillary force given by each inside meniscus, owing to the enhanced protrusion with a large spacing; the latter increases the total number of these menisci. However, both ways are limited by the overall size of the hairy surface. In §4, we will discuss how to obtain an optimum design for a hairy surface floating on water by adjusting the cylinder spacing.

4. Optimum design of hairy surfaces

As pointed out in §3, the maximum load-carrying position of a hairy surface is determined by the outside meniscus. Thus, for a given width and Bond number, the buoyant force produced by the outside menisci is fixed and the optimum design of a hairy surface can be obtained by adjusting the number and/or spacing of the cylinders. For the legs and wings of some insects (e.g. water striders, figure 1), it is meaningful to optimize the spacing between their setae so as to generate the maximum supporting force per unit area. Therefore, a smaller part of the legs will be wetted during a stroke when a water strider flees away and similarly, the contact area will also be smaller when the wing surface is impacted by a droplet (figure 1*a*,*b*). This will undoubtedly reduce the adhesion and energy dissipation during the movement of insects on water or flying in a very humid environment. On the other hand, for the design of a mini-raft of given width $\tilde{W}$, it is important to optimize the cylinder number for maximizing the load-carrying capacity of the raft. Note that $\tilde{W} = 2\tilde{\delta} \cdot (N - 1)$ (figure 2*a*). The total maximum load-carrying capacity given by the raft in equation (3.10) is obtained by an optimum design of the inside cylinders,

$$\tilde{F}_{\mathrm{cpc,max}} = \tilde{F}_{1,\mathrm{max}} + \frac{\tilde{W}}{2} \cdot \left(\frac{\tilde{F}_2}{\tilde{\delta}}\right)_{\mathrm{max}}. \tag{4.1}$$

From equation (4.1), we can see that the two optima, i.e. the optimum of the force per unit width and the optimum in the total force are consistent with each other. The optimum of the force per unit width generally leads to the optimum of the total force over a given width. Therefore, the study in the following sections is focused on the former optimum, i.e. maximizing $\tilde{F}_2/\tilde{\delta}$. As

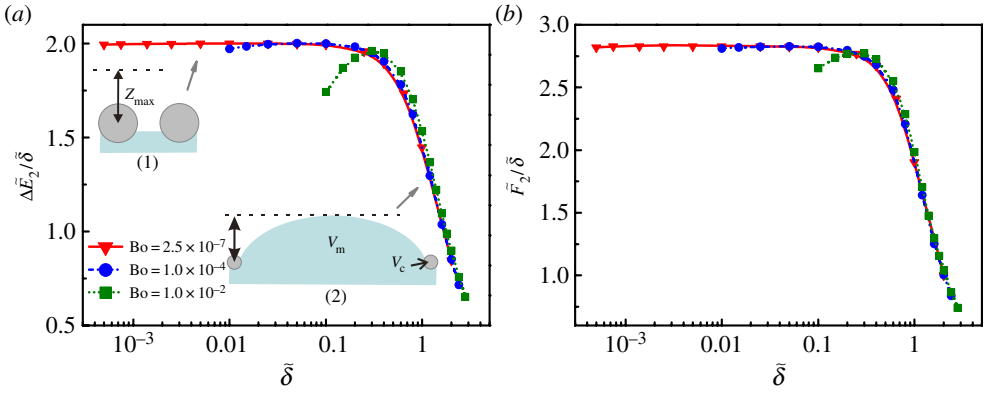

Figure 7. Dependence of $\Delta\tilde{E}_2/\tilde{\delta}$ and $\tilde{F}_2/\tilde{\delta}$ on $\tilde{\delta}$ at the maximum load-carrying position with different Bond numbers ($\theta_Y = 105^\circ$). Insets in (*a*) represent the schematics of the inside meniscus at (1) small (e.g. $\tilde{\delta} = 0.005$) and (2) large (e.g. $\tilde{\delta} = 1$) spacings. Z_{max} in the insets denotes the displacement at the maximum load-carrying position. V_m and V_c are the volumes of the protruded meniscus and the cylinder, respectively. (Online version in colour.)

illustrated by equations (2.3) and (3.8), $\tilde{F}_2$ depends on the parameters $\tilde{\delta}$, Bo and θ_Y. Therefore, the optimum design of a hairy surface can be obtained by adjusting these parameters, as will now be discussed.

(a) Influence of hair spacing

We first investigate the dependence of $\Delta\tilde{E}_2$ and $\tilde{F}_2$ per unit spacing (i.e. $\Delta\tilde{E}_2/\tilde{\delta}$ and $\tilde{F}_2/\tilde{\delta}$) on $\tilde{\delta}$ at the maximum load-carrying position (e.g. for $\theta_Y = 105^\circ$, $\theta_1 \sim 165^\circ$), which is plotted in figure 7 for three chosen Bond numbers (e.g. $\mathrm{Bo} = 2.5 \times 10^{-7}$, $\mathrm{Bo} = 1.0 \times 10^{-4}$ and $\mathrm{Bo} = 1.0 \times 10^{-2}$). As shown in figure 7*a*,*b*, $\Delta\tilde{E}_2/\tilde{\delta}$ and $\tilde{F}_2/\tilde{\delta}$ show consistent results with each other: they both increase dramatically with the decrease of $\tilde{\delta}$ when $\tilde{\delta}$ is large (e.g. $\tilde{\delta} > 0.1$), reach a maximum and then decrease slightly with further decrease of $\tilde{\delta}$ when $\tilde{\delta}$ is very small (e.g. $\tilde{\delta} < 0.1$). It is seen that, for a large cylinder spacing, the inside meniscus protrudes upward significantly (see the inset 2 in figure 7*a*) and generates a vertical supporting force comparable with that of the outside meniscus (figure 6). For a small spacing, owing to the much smaller pressure difference across the meniscus than the maximum Laplace pressure that can be provided (see equations (2.6) and (2.7)), the meniscus is almost planar (see the inset 1 in figure 7*a*). Thus, the vertical supporting force given by each inside meniscus is negligible when compared with the outside meniscus (figure 6).

According to the generalized Archimedes' principle [34], the total buoyant force provided by the cylinders is proportional to the total volume of the liquid replaced by the cylinders and the menisci. Estimating $\tilde{F}_2/\tilde{\delta}$ at the maximum load-carrying position from the volume of the replaced liquid gives

$$\frac{\tilde{F}_2}{\tilde{\delta}} \propto Z_{max}L - \frac{V_m}{\delta} - \frac{DeV_c}{\delta}, \tag{4.2}$$

where Z_{max} is the displacement at the maximum load-carrying position, V_m and V_c are the volumes of the protruded meniscus and the cylinder, respectively (see the insets in figure 7*a*). Equation (4.2) gives a good approximation to the buoyant force per unit width, especially for the thin cylinders.

As indicated by the insets in figure 7*a* and Laplace equation (2.6), the larger the spacing is, the smaller the Laplace pressure that can be provided, and the higher the inside meniscus that will protrude upward. Thus, V_m/δ decreases with the spacing δ and approaches zero as $\delta \to 0$. In fact, for a large spacing, the protruded meniscus between cylinders actually reduces the replaced liquid volume per unit width and, therefore, reduces $\tilde{F}_2/\tilde{\delta}$, as shown in figure 7*b*. Note that,

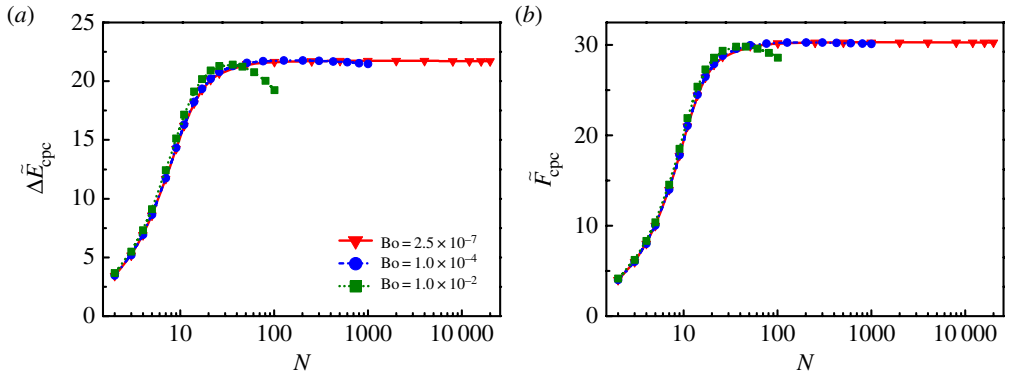

Figure 8. Plots $\Delta\tilde{E}_{cpc}$ and $\tilde{F}_{cpc}$ for a hairy surface of width $\tilde{W} = 10$ as a function of the cylinder number N at the maximum load-carrying position. (Online version in colour.)

although the cylinder material is heavier than water ($De = 1.2$), DeV_c is generally much smaller than the liquid volume replaced by the meniscus. When the spacing is very small, the vertical capillary force given by the meniscus per unit width tends to be constant and proportional to $Z_{max}L$ (see equation (4.2)). On the other hand, the gravity of the cylinder becomes relatively more significant, which results in slight decreases of $\Delta\tilde{E}_2/\tilde{\delta}$ and $\tilde{F}_2/\tilde{\delta}$. The thicker the cylinder, the more pronounced the drops of $\Delta\tilde{E}_2/\tilde{\delta}$ and $\tilde{F}_2/\tilde{\delta}$, as seen in figure 7*a*,*b*, respectively.

If the width of the hairy surface is fixed (e.g. when designing a cylinder raft), then the spacing between cylinders determines the number of the cylinders that can be used. To see the optimized design more clearly, we plot the load-carrying capacity and the corresponding free energy change $\tilde{F}_{cpc}$ and $\Delta\tilde{E}_{cpc}$ in figure 8 for a cylinder raft of width $\tilde{W} = 10$ with three different Bond numbers (e.g. $Bo = 2.5 \times 10^{-7}$, $Bo = 1.0 \times 10^{-4}$ and $Bo = 1.0 \times 10^{-2}$). As shown in figure 8, we find consistent results between $\tilde{F}_{cpc}$ and $\Delta\tilde{E}_{cpc}$ again. When the cylinder number is low, they first increase quickly with the cylinder number until a maximum value is reached, and then decrease slightly with further increase of N. Both figures 7 and 8 prove that there exists an optimized design for the hairy surface. Note that at the maximum load-carrying position, the contributions from the outside menisci to the free energy change and force are fixed. The above two optima (figures 7 and 8) are consistent with each other and they both lead to an optimized spacing of the cylinders, as shown in equation (4.1).

This optimized spacing between cylinders can be obtained by letting the derivatives of $\Delta\tilde{E}_2/\tilde{\delta}$ and $\tilde{F}_2/\tilde{\delta}$ with respect to $\tilde{\delta}$ be 0. These maximum values are denoted by $(\Delta\tilde{E}_2/\tilde{\delta})_{max}$ and $(\tilde{F}_2/\tilde{\delta})_{max}$, respectively.

$$\frac{\partial}{\partial\tilde{\delta}}\left(\frac{\Delta\tilde{E}_2}{\tilde{\delta}}\right) = -\frac{\Delta\tilde{E}_2}{\tilde{\delta}^2} + \frac{1}{\tilde{\delta}}\frac{\partial\Delta\tilde{E}_2}{\partial\theta_2}\Big/\frac{\partial\tilde{\delta}}{\partial\theta_2} = 0 \tag{4.3}$$

and

$$\frac{\partial}{\partial\tilde{\delta}}\left(\frac{\tilde{F}_2}{\tilde{\delta}}\right) = -\frac{\tilde{F}_2}{\tilde{\delta}^2} + \frac{1}{\tilde{\delta}}\frac{\partial\tilde{F}_2}{\partial\theta_2}\Big/\frac{\partial\tilde{\delta}}{\partial\theta_2} = 0. \tag{4.4}$$

Solutions to equations (4.3) and (4.4) give the critical values of $\tilde{\delta}$, or $\tilde{\delta}_{cri}$, which correspond to the optimized spacing of the inside cylinders. The detailed procedure to solve equations (4.3) and (4.4) can be found in appendix B. Then, the maximum values of $\Delta\tilde{E}_2/\tilde{\delta}$ and $\tilde{F}_2/\tilde{\delta}$ can be calculated by substituting $\tilde{\delta}_{cri}$ into equations (3.6) and (3.8), respectively. Note that the values of $\tilde{\delta}_{cri}$ given by equations (4.3) and (4.4) are not necessarily the same but should be close with each other based the concept that both free energy and force analyses give consistent results. The range between those two values represents an optimized design by which both maximum load-carrying capacity and high mechanical stability can be obtained. We plot $\tilde{\delta}_{cri}$ as a function of the Bond number for three different Young contact angles θ_Y in figure 9. For all θ_Y, both values of

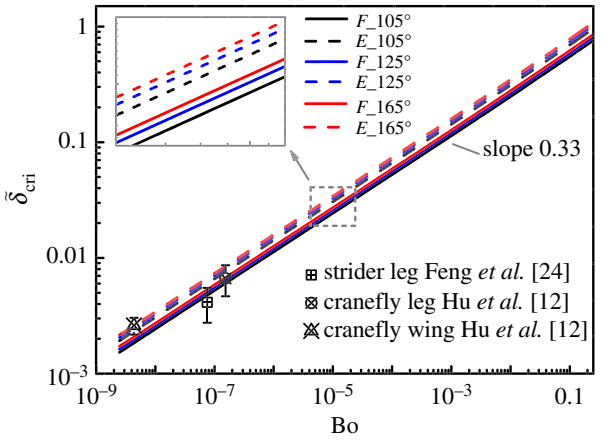

Figure 9. Dependence of $\tilde{\delta}_{cri}$ on Bo with respect to different Young contact angles: $\theta_Y = 10^\circ$, $\theta_Y = 125^\circ$ and $\theta_Y = 165^\circ$. Solid lines denote $\tilde{\delta}_{cri}$ which are obtained by the force analysis; dashed lines denote $\tilde{\delta}_{cri}$ which are obtained by the free energy analysis. The data of the setae on water strider's legs are from Feng *et al.* [24] and the data of the hairs on a cranefly wing and leg are from Hu *et al.* [12]. The inset shows a magnified view of the plot in the region of the dashed box. (Online version in colour.)

$\tilde{\delta}_{cri}$ obtained by equations (4.3) and (4.4) are plotted. The region between these two lines can be a guide for designing hairy surfaces with both high load-carrying capacity and floating stability. It is surprising to find that the optimized spacing $\tilde{\delta}_{cri}$ follows a simple power law with the Bond number with the fitted exponent equal to 1/3, that is,

$$\tilde{\delta}_{cri} \propto \mathrm{Bo}^{1/3}. \tag{4.5}$$

The scaling law (4.5) is valid over an enormous range of Bond numbers and contact angles, because of the same mechanism, i.e. the compromise between the vertical capillary force and the gravity, as indicated by equation (4.2). The data points of the cone-shaped setae/hairs on the legs of water striders and on a cranefly wing and leg are also included in figure 9. Those data agree closely with our theoretical optimization prediction. Therefore, for the first time, we show that the setae on the legs of water striders are arranged in such an optimized way that those setae can give both high support and floating stability for water striders' legs. The spacing of the hairs on the wings of a fly is optimized so that water droplets will not be penetrated easily by those hairs during an impact and more importantly, will be repelled away easily owing to a reduced base contact area with the wing surface. Though the load-carrying capacity only decreases slightly when further decreasing the seta spacing, more densely packed setae will definitely cost more biological energy, and increase the adhesion and energy dissipation during the movement of water striders on water.

(b) Influences of contact angle and Bond number

From §4*a*, we have learned that, for cylinders with a given Bond number Bo and contact angle θ_Y, the optimized spacing of these cylinders can be obtained by equations (4.3) and (4.4). At the optimized cylinder spacing, i.e. $\tilde{\delta}_{cri}$, the hairy surface exhibits the maximum load-carrying capacity per unit width, i.e. $(\tilde{F}_2/\tilde{\delta})_{max}$. In the following, we will investigate the influences of θ_Y and Bo on $(\Delta\tilde{E}_2/\tilde{\delta})_{max}$ and $(\tilde{F}_2/\tilde{\delta})_{max}$ at the optimized spacing, which are obtained by substituting $\tilde{\delta}_{cri}$ into equations (3.6) and (3.8). Plots of $(\Delta\tilde{E}_2/\tilde{\delta})_{max}$ and $(\tilde{F}_2/\tilde{\delta})_{max}$ as functions of θ_Y are shown in figure 10. It is seen that, for very thin cylinders (e.g. $\mathrm{Bo} = 2.5 \times 10^{-7}$), both $(\Delta\tilde{E}_2/\tilde{\delta})_{max}$ and $(\tilde{F}_2/\tilde{\delta})_{max}$ change very slightly with the increase of θ_Y. The improvement of those maximum values owing to the increase of θ_Y becomes more pronounced for thick cylinders (e.g. $\mathrm{Bo} = 1.0 \times 10^{-2}$). It is consistent with the previous results reported about a single cylinder floating on

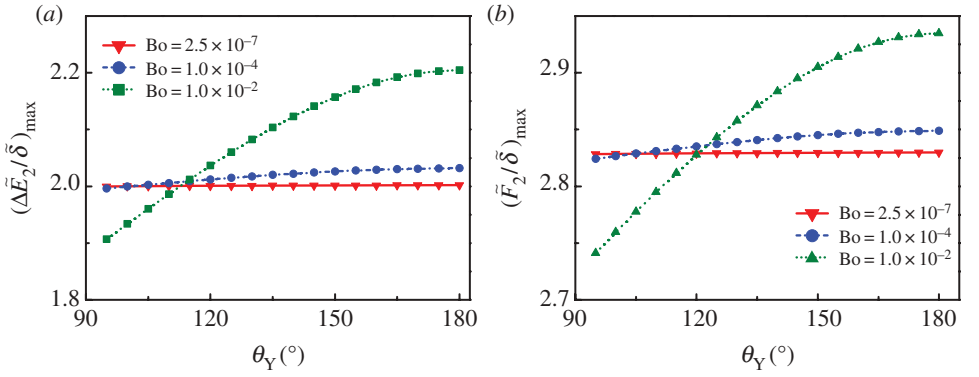

Figure 10. The maximum values of $\Delta\tilde{E}_2/\tilde{\delta}$ and $\tilde{F}_2/\tilde{\delta}$ as functions of θ_Y with respect to different Bond numbers: $Bo = 2.5 \times 10^{-7}$, $Bo = 1.0 \times 10^{-4}$ and $Bo = 1.0 \times 10^{-2}$. (Online version in colour.)

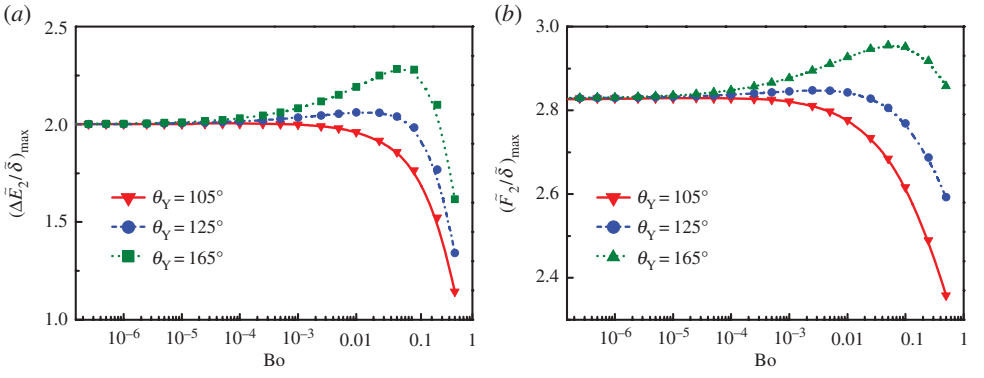

Figure 11. The maximum values of $\Delta\tilde{E}_2/\tilde{\delta}$ and $\tilde{F}_2/\tilde{\delta}$ as functions of the Bond number Bo with different Young contact angles: $Bo = 2.5 \times 10^{-7}$, $Bo = 1.0 \times 10^{-4}$ and $Bo = 1.0 \times 10^{-2}$. (Online version in colour.)

water [26,28]. Plots of $(\Delta\tilde{E}_2/\tilde{\delta})_{max}$ and $(\tilde{F}_2/\tilde{\delta})_{max}$ as functions of Bo are shown in figure 11. For low hydrophobicity (e.g. $\theta_Y = 105°$), the maximum values of $\Delta\tilde{E}_2/\tilde{\delta}$ and $\tilde{F}_2/\tilde{\delta}$ first decrease slightly as the increase in the Bond number and decrease quickly when Bo is higher than 1.0×10^{-4}. If the cylinders are superhydrophobic (e.g. $\theta_Y = 165°$), then the maximum values of $\Delta\tilde{E}_2/\tilde{\delta}$ and $\tilde{F}_2/\tilde{\delta}$ reach a maximum at $Bo \sim 0.1$. In other words, it is not necessary for hairy surfaces made of very thin cylinders (e.g. $Bo < 1.0 \times 10^{-4}$) to be superhydrophobic. If the cylinders are thick (e.g. $Bo > 1.0 \times 10^{-4}$), then superhydrophobicity can further increase the load-carrying capacity of hairy surfaces.

5. Concluding remarks

We have investigated the mechanism and optimization of hairy surfaces made from parallel cylinders floating on water to obtain the maximum load-carrying capacity and mechanical stability. It has been shown that the optimum design is achieved by adjusting the parameters, i.e. the spacing, the Bond number and the Young contact angle of the cylinders. For a hairy surface of a given width and Bond number, there exists an optimum cylinder spacing at which both high load-carrying capacity and strong floating stability can be obtained. The optimization arises from a compromise between the vertical capillary force given by the menisci and the gravity of the cylinders. The decrease in the cylinder spacing contributes to the increase in the vertical capillary

force of the meniscus per unit width, but the increased gravity will reduce the increase in the total buoyant force. Moreover, for thin cylinders (e.g. $\mathrm{Bo} < 1.0 \times 10^{-4}$), surface hydrophobicity plays a negligible role in the increase of the load-carrying capacity. Otherwise, if $\mathrm{Bo} > 1.0 \times 10^{-4}$, then superhydrophobicity can be used to further improve the performance of hairy surfaces floating on water. We clarify that the setae/hairs on some insects' legs or wings follow the optimization principle we find here. Though the decrease in the buoyant force given by the inside meniscus per unit width is slight owing to the gravity for the setae, it is not necessary for them to grow more densely, or otherwise, it will cost more biological energy and may even harm the flexibility of the legs or wings.

In this work, the optimization design of a hairy surface is obtained and analysed at the position where the supporting force given by the outside menisci reaches a maximum. The choice of this position is based on the fact that the collapse of the outside meniscus generally leads to the failure of the whole cylinder raft. This does not exclude the possibility that locally wetting transition may happen as a result of, e.g. condensation [42], or an extremely strong impact and, then, induce the submersion of the whole surface. However, this is out of the range of the present topic. Note that we investigate a hairy surface model made from parallel cylinders and that both three-dimensional and hydrodynamic effects are neglected. The same optimization principle can also be applied to the design of rafts made from cylinders with arbitrary orientations and/or cross-sectional shapes, which requires a compromise of the vertical capillary force and the gravity per unit area. However, more integrated numerical methods are needed to characterize the pore structures and quantify the capillary and gravity forces generated by arbitrary cylinder geometries. This is because both the orientations and the cross-sectional shapes of the cylinders/fibres affect the capillary force [32,33]. Therefore, our theory can be a practical guide for designing micro-cylinder rafts with high load-carrying capacity.

The theory developed in this work can also be used for analysing the lifting process of hairy surfaces, which can be regarded as an antisymmetrical process to the sinking one with respect to the neutral position (figures 3 and 4). Thus, the optimization design of hairy surfaces for a maximum load-carrying capacity, on the other hand, increases the force and energy needed to lift a hairy surface from water. It is generally seen that though most insects' wings are superhydrophobic, it is not easy to lift the wing up once it is fully contacted with water surface. However, for insects living on water, low energy dissipation is needed for them to lift their legs from water so that they can quickly move and flee away from possible threats [10]. To meet such requirement, the setae on their legs need to be arranged in a special way, e.g. on a convex contour or circle (figure 1), rather than on a flat surface. During a lifting process, the convex contour enables the detaching of the contact menisci to happen gradually from both sides of a hairy surface instead of the simultaneous detachment of all the menisci, which will greatly reduce the force and energy needed to lift a hairy surface from water. From another point of view, those setae, together with sub-scale groove structures and wax surface, render water striders' legs superhydrophobic [24]. The superhydrophobicity decreases the adhesive force between the convex contour and water surface [27]. However, how the convex contour constructed by parallel cylinders influences the lifting process of the wetting contact lines needs further investigation.

Funding statement. We acknowledge Major State Basic Research Development Program of China (grant no. 2011CB013101), National Natural Science Foundation of China (NSFC) under grant nos. 11225208, 10872003 and 11172001, The Alexander von Humboldt (AvH) foundation in Germany to support this work through project 'Mechanics theory of materials with complex surfaces and its applications' in the frame of the AvH program for funding a research group linkage.

Appendix A. Buoyant force

In appendix A, we give the detailed procedure to obtain equation (3.8) by a combination of equations (3.1)–(3.5) and (3.7). According to equations (3.1)–(3.5), differentiating the free energy

changes with respect to θ_i $(i=1,2)$ yields

$$\frac{\partial \tilde{E}_{S1}}{\partial \theta_1} = -2\sqrt{\mathrm{Bo}}(\cos\theta_Y + \cos\theta_1) + \frac{\sqrt{2}\sin\psi_1}{\sqrt{1+\cos\psi_1}}, \tag{A 1}$$

$$\frac{\partial \tilde{E}_{G1}}{\partial \theta_1} = \tilde{h}_1 \frac{\partial \tilde{h}_1}{\partial \theta_1}\left(\frac{2-\tilde{h}_1^2}{\sqrt{4-\tilde{h}_1^2}} + 2\sqrt{\mathrm{Bo}}\sin\theta_1\right) + \mathrm{Bo}^{3/2}(\theta_1\sin\theta_1 - \sin^2\theta_1\cos\theta_1)$$
$$+ \tilde{h}_1^2\sqrt{\mathrm{Bo}}\cos\theta_1 - \mathrm{Bo}\left[\frac{\partial \tilde{h}_1}{\partial \theta_1}(-\theta_1 + \sin\theta_1\cos\theta_1) - 2\tilde{h}_1\sin^2\theta_1\right], \tag{A 2}$$

$$\frac{\partial \tilde{E}_{Gs}}{\partial \theta_i} = -\pi\,\mathrm{Bo}De\frac{\partial \tilde{Z}}{\partial \theta_i} \quad (i=1,2), \tag{A 3}$$

$$\frac{\partial \tilde{E}_{S2}}{\partial \theta_2} = -2\sqrt{\mathrm{Bo}}\cos\theta_Y - \sqrt{2}\eta\left\{\frac{\sin\psi_2}{(c_2^2-1)\sqrt{c_2-\cos\psi_2}}\frac{c_2}{\theta_2}\right.$$
$$\left. + \frac{\mathbf{EE}(\psi_2/2, 2/(1-c_2))}{(c_2+1)\sqrt{c_2-1}}\frac{c_2}{\theta_2} - \frac{1}{\sqrt{c_2-\cos\psi_2}}\right\} \tag{A 4}$$

and

$$\frac{\partial \tilde{E}_{G2}}{\partial \theta_2} = \sqrt{\mathrm{Bo}}\cos\theta_2\tilde{h}_2^2 + \sqrt{\mathrm{Bo}}\sin\theta_2\tilde{h}_2\frac{\partial \tilde{h}_2}{\partial \theta_2} + \mathrm{Bo}(\theta_2 - \cos\theta_2\sin\theta_2)\frac{\partial \tilde{Z}}{\partial \theta_2}$$
$$+ \sqrt{2}\eta\left[\sqrt{c_2-\cos\psi_2}\cos\psi_2\right.$$
$$\left. + \frac{(1-c_2)\mathbf{EE}(\psi_2/2, 2/(1-c_2)) + c_2\mathbf{EF}(\psi_2/2, 2(1-c_2))}{\sqrt{c_2-1}}\frac{\partial c_2}{\partial \theta_2}\right]. \tag{A 5}$$

According to equation (2.4), differentiating the displacement with respect to θ_i $(i=1,2)$ yields

$$\frac{\partial \tilde{Z}}{\partial \theta_i} = \frac{\partial \tilde{h}_i}{\partial \theta_i} + \sqrt{\mathrm{Bo}}\sin\theta_i \quad (i=1,2). \tag{A 6}$$

With $\tilde{h}_2 = \eta\sqrt{2}\sqrt{c_2+\cos(\theta_Y+\theta_2)}$ and equation (2.5), we have

$$\frac{\partial c_2}{\partial \theta_2} = \tilde{h}_2\frac{\partial \tilde{h}_2}{\partial \theta_2} + \sin(\theta_Y+\theta_2) \tag{A 7}$$

and

$$\sqrt{2}\sqrt{\mathrm{Bo}}\cos\theta_2 = \eta\left\{-\frac{\cos\psi_2}{\sqrt{c_2-\cos\psi_2}} + \frac{c_2\sin\psi_2}{(c_2^2-1)\sqrt{c_2-\cos\psi_2}}\frac{\partial c_2}{\partial \theta_2} + \right.$$
$$\left. + \frac{c_2\mathbf{EE}(\psi_2/2, 2/(1-c_2)) - (1+c_2)\mathbf{EF}(\psi_2/2, 2/(1-c_2))}{(c_2+1)\sqrt{c_2-1}}\frac{\partial c_2}{\partial \theta_2}\right\}. \tag{A 8}$$

By substituting equations (A 1)–(A 6) into equation (3.7) and combining equations (A 6) and (A 7), we get equation (3.8) after certain algebraic calculations.

Appendix B. Critical spacing

In appendix B, we give the detailed procedure to obtain $\tilde{\delta}_{cri}$ by solving equations (4.3) and (4.4). For a given Bond number Bo and Young contact angle θ_Y, we calculate the optimized cylinder spacings for maximum buoyant force and free energy change per unit width at the maximum load-carrying position, respectively. We rewrite equation (2.5) as

$$\tilde{\delta} = \sqrt{\mathrm{Bo}}\cos\theta_2 - \eta\frac{\sqrt{2}}{c_2-1}\left[(c_2-1)\mathbf{EE}\left(\frac{\psi_2}{2}, \frac{2}{c_2-1}\right) - c_2\mathbf{EF}\left(\frac{\psi_2}{2}, \frac{2}{c_2-1}\right)\right]. \tag{B 1}$$

At the maximum load-carrying position, θ_1 and $\tilde{Z}$ are constant and only depends on the Bond number Bo and Young contact angle θ_Y. Thus, by equation (2.4), we have

$$\frac{\partial \tilde{h}_2}{\partial \theta_2} = -\sqrt{\mathrm{Bo}}\sin\theta_2. \tag{B 2}$$

Substituting equation (B 2) into equation (A 7) yields

$$\frac{\partial c_2}{\partial \theta_2} = -\sqrt{\mathrm{Bo}}\tilde{h}_2\sin\theta_2 + \sin(\theta_Y + \theta_2). \tag{B 3}$$

With equation (B 3), differentiating equation (B 1) with respect to θ_2 yields

$$\frac{\partial \tilde{\delta}}{\partial \theta_2} = \sqrt{\mathrm{Bo}}\cos\theta_2 + \eta\left\{\frac{\cos\psi_2}{\sqrt{2(c_2-\cos\psi_2)}} - \frac{\partial c_2}{\partial \theta_2}\right.$$
$$\left.\cdot\frac{c_2\sin\psi_2 + \sqrt{(c_2-1)(c_2-\cos\psi_2)}[c_2\mathbf{EE}(\psi_2/2, 2/(1-c_2)) - (1+c_2)\mathbf{EF}(\psi_2/2, 2/(1-c_2))]}{(c_2^2-1)\sqrt{2(c_2-\cos\psi_2)}}\right\}. \tag{B 4}$$

Equation (4.3) is rewritten as

$$\frac{\partial}{\partial \tilde{\delta}}\left(\frac{\Delta\tilde{E}_2}{\tilde{\delta}}\right) = -\frac{\Delta\tilde{E}_{S2} + \Delta\tilde{E}_{G2} + \Delta\tilde{E}_{Gs}}{\tilde{\delta}^2} + \frac{1}{\tilde{\delta}}\left(\frac{\partial\tilde{E}_{S2}}{\partial\theta_2} + \frac{\partial\tilde{E}_{G2}}{\partial\theta_2} + \frac{\partial\tilde{E}_{Gs}}{\partial\theta_2}\right)\Big/\frac{\partial\tilde{\delta}}{\partial\theta_2} = 0, \tag{B 5}$$

where

$$\frac{\partial\tilde{E}_{S2}}{\partial\theta_2} = -2\sqrt{\mathrm{Bo}}\cos\theta_Y - 2\frac{\partial\tilde{\delta}}{\partial\theta_2} + 2\eta\left\{\frac{1}{\sqrt{2(c_2-\cos\psi_2)}} - \frac{\partial c_2}{\partial\theta_2}\right.$$
$$\left.\cdot\frac{\sqrt{(c_2-1)(c_2-\cos\psi_2)}\mathbf{EE}(\psi_2/2, 2/(1-c_2)) + \sin\psi_2}{(c_2^2-1)\sqrt{2(c_2-\cos\psi_2)}}\right\}, \tag{B 6}$$

$$\frac{\partial\tilde{E}_{G2}}{\partial\theta_2} = \sqrt{\mathrm{Bo}}\cos\theta_2\tilde{h}_2^2 + \eta\sqrt{2}\left\{\sqrt{c_2-\cos\psi_2}\cos\psi_2\right.$$
$$\left.+\frac{\partial c_2}{\partial\theta_2}\cdot\frac{(1-c_2)\mathbf{EE}(\psi_2/2, 2/(1-c_2)) + c_2\mathbf{EF}(\psi_2/2, 2/(1-c_2))}{\sqrt{c_2-1}}\right\} \tag{B 7}$$

and

$$\frac{\partial\tilde{E}_{Gs}}{\partial\theta_2} = 0. \tag{B 8}$$

By combining equations (B 3)–(B 8), we can get the critical cylinder spacing satisfying equation (4.3) after simple numerical calculation. Differentiating equation (3.8) with respect to θ_2 yields

$$\frac{\partial\tilde{F}_2}{\partial\theta_2} = -2\cos(\theta_2+\theta_Y) + 2\sqrt{\mathrm{Bo}}\cos\theta_2\tilde{h}_2. \tag{B 9}$$

By substituting equations (B 4) and (B 9) into equation (4.4), we get the critical cylinder spacing satisfying equation (4.4) after a simple numerical calculation.

References

1. Rothstein JP. 2010 Slip on superhydrophobic surfaces. *Annu. Rev. Fluid Mech.* **42**, 89–109. (doi:10.1146/annurev-fluid-121108-145558)
2. Bhushan B, Jung YC, Koch K. 2009 Micro-, nano- and hierarchical structures for superhydrophobicity, self-cleaning and low adhesion. *Phil. Trans. R. Soc. A* **367**, 1631–1672. (doi:10.1098/rsta.2009.0014)
3. Liu X, Liang Y, Zhou F, Liu W. 2012 Extreme wettability and tunable adhesion: biomimicking beyond nature? *Soft Matter* **8**, 2070–2086. (doi:10.1039/c1sm07003g)
4. Feng L *et al.* 2002 Super-hydrophobic surfaces: from natural to artificial. *Adv. Mater.* **14**, 1857–1860. (doi:10.1002/adma.200290020)

5. Bhushan B. 2009 Biomimetics: lessons from nature—an overview. *Phil. Trans. R. Soc. A* **367**, 1445–1486. (doi:10.1098/rsta.2009.0011)
6. Yan YY, Gao N, Barthlott W. 2011 Mimicking natural superhydrophobic surfaces and grasping the wetting process: a review on recent progress in preparing superhydrophobic surfaces. *Adv. Colloid Interface Sci.* **169**, 80–105. (doi:10.1016/j.cis.2011.08.005)
7. Koch K, Barthlott W. 2009 Superhydrophobic and superhydrophilic plant surfaces: an inspiration for biomimetic materials. *Phil. Trans. R. Soc. A* **367**, 1487–1509. (doi:10.1098/rsta.2009.0022)
8. Neinhuis C, Barthlott W. 1997 Characterization and distribution of water-repellent, self-cleaning plant surfaces. *Ann. Bot.* **79**, 667–677. (doi:10.1006/anbo.1997.0400)
9. Gao XF, Jiang L. 2004 Water-repellent legs of water striders. *Nature* **432**, 36. (doi:10.1038/432036a)
10. Hu DL, Chan B, Bush JWM. 2003 The hydrodynamics of water strider locomotion. *Nature* **424**, 663–666. (doi:10.1038/nature01793)
11. Wagner T, Neinhuis C, Barthlott W. 1996 Wettability and contaminability of insect wings as a function of their surface sculptures. *Acta Zool.* **77**, 213–225. (doi:10.1111/j.1463-6395.1996.tb01265.x)
12. Hu HMS, Watson GS, Cribb BW, Watson JA. 2011 Non wetting wings and legs of the cranefly aided by fine structures of the cuticle. *J. Exp. Biol.* **214**, 915–920. (doi:10.1242/jeb.051128)
13. Thorpe WH, Crisp DJ. 1947 Studies on plastron respiration I. The biology of Aphelocheirus [Hemiptera, Aphelocheiridae (Naucoridae)] and the mechanism of plastron retention. *J. Exp. Biol.* **24**, 227–269.
14. Thorpe WH, Crisp DJ. 1949 Studies on plastron respiration IV. plastron respiration in the Coleoptera. *J. Exp. Biol.* **26**, 219–260.
15. Flynn MR, Bush JWM. 2008 Underwater breathing: the mechanics of plastron respiration. *J. Fluid Mech.* **608**, 275–296. (doi:10.1017/S0022112008002048)
16. Marmur A, Ras RHA. 2011 The porous nano-fibers raft: analysis of load-carrying mechanism and capacity. *Soft Matter* **7**, 7382–7385. (doi:10.1039/c1sm05156c)
17. Pan QM, Wang M. 2009 Miniature boats with striking loading capacity fabricated from superhydrophobic copper meshes. *ACS Appl. Mater. Interfaces* **1**, 420–423. (doi:10.1021/am800116d)
18. Jiang ZX, Geng L, Huang YD. 2010 Design and fabrication of hydrophobic copper mesh with striking loading capacity and pressure resistance. *J. Phys. Chem. C* **114**, 9370–9378. (doi:10.1021/jp1009516)
19. Aussillous P, Quéré D. 2006 Properties of liquid marbles. *Proc. R. Soc. A* **462**, 973–999. (doi:10.1098/rspa.2005.1581)
20. Jiang ZX, Geng L, Huang YD. 2010 Fabrication of superhydrophobic 3-D braided carbon fiber fabric boat. *Mater. Lett.* **64**, 2441–2443. (doi:10.1016/j.matlet.2010.08.015)
21. Jin H, Kettunen M, Laiho A, Pynnönen H, Paltakari J, Marmur A, Ikkala O, Ras RHA. 2011 Superhydrophobic and superoleophobic nanocellulose aerogel membranes as bioinspired cargo carriers on water and oil. *Langmuir* **27**, 1930–1934. (doi:10.1021/la103877r)
22. Hsu SH, Woan K, Sigmund W. 2011 Biologically inspired hairy structures for superhydrophobicity. *Mater. Sci. Eng. R* **72**, 189–201. (doi:10.1016/j.mser.2011.05.001)
23. Blow ML, Yeomans JM. 2010 Superhydrophobicity on hairy surfaces. *Langmuir* **26**, 16 071–16 083. (doi:10.1021/la101847b)
24. Feng XQ, Gao XF, Wu ZN, Jiang L, Zheng QS. 2007 Superior water repellency of water strider legs with hierarchical structures: experiments and analysis. *Langmuir* **23**, 4892–4896. (doi:10.1021/la063039b)
25. Vella D, Lee DG, Kim HY. 2006 The load supported by small floating objects. *Langmuir* **22**, 5979–5981. (doi:10.1021/la060606m)
26. Liu JL, Feng XQ, Wang GF. 2007 Buoyant force and sinking conditions of a hydrophobic thin rod floating on water. *Phys. Rev. E* **76**, 066103. (doi:10.1103/PhysRevE.76.066103)
27. Lee DG, Kim HY. 2009 The role of superhydrophobicity in the adhesion of a floating cylinder. *J. Fluid Mech.* **624**, 23–32. (doi:10.1017/S002211200900593X)
28. Su YW, Ji BH, Zhang K, Gao HJ, Huang YG, Hwang K. 2010 Nature's design of hierarchical superhydrophobic surfaces of a water strider for low adhesion and low-energy dissipation. *Langmuir* **26**, 18926–18937. (doi:10.1021/la103442b)
29. Vella D. 2008 Floating objects with finite resistance to bending. *Langmuir* **24**, 8701–8706. (doi:10.1021/la800245k)

30. Zheng QS, Yu Y, Feng XQ. 2009 The role of adaptive-deformation of water strider leg in its walking on water. *J. Adhes. Sci. Technol.* **23**, 493–501. (doi:10.1163/156856108X379155)
31. Ji XY, Wang JW, Feng XQ. 2012 Role of flexibility in the water repellency of water strider legs: theory and experiment. *Phys. Rev. E* **85**, 021607. (doi:10.1103/PhysRevE.85.021607)
32. Emami, B, Tafreshi, HV, Gad-el-Hak M, Tepper GC. 2012 Effect of fiber orientation on shape and stability of air–water interface on submerged superhydrophobic electrospun thin coatings. *J. Appl. Phys.* **111**, 064325. (doi:10.1063/1.3697895)
33. Emami B, Tafreshi HV. 2012 Optimizing fiber cross-sectional shape for improving stability of air–water interface over superhydrophobic fibrous coatings. *Appl. Phys. Lett.* **100**, 193104. (doi:10.1063/1.4711800)
34. Keller JB. 1998 Surface tension force on a partly submerged body. *Phys. Fluids* **10**, 3009–3010. (doi:10.1063/1.869820)
35. Bhatnager R, Finn R. 2006 Equilibrium configurations of an infinite cylinder in an unbounded fluid. *Phys. Fluids* **18**, 047103. (doi:10.1063/1.2185661)
36. Vella D, Metcalfe PD, Whittaker RJ. 2006 Equilibrium conditions for the floating of multiple interfacial objects. *J. Fluid Mech.* **549**, 215–224. (doi:10.1017/S0022112005008013)
37. Wei PJ, Shen YX, Lin JF. 2009 Characteristics of water strider legs in hydrodynamic situations. *Langmuir* **25**, 7006–7009. (doi:10.1021/la900185a)
38. Rapacchietta AV, Neumann AW, Omenyi SN. 1977 Force and free-energy analyses of small particles at fluid interfaces. I. cylinders. *J. Colloid Interface Sci.* **59**, 541–554. (doi:10.1016/0021-9797(77)90050-9)
39. Marmur A. 2003 Wetting on hydrophobic rough surfaces: to be heterogeneous or not to be? *Langmuir* **19**, 8343–8348. (doi:10.1021/la0344682)
40. Patankar NA. 2004 Transition between superhydrophobic states on rough surfaces. *Langmuir* **20**, 7097–7102. (doi:10.1021/la049329e)
41. Xue YH, Chu SG, Lv PY, Duan HL. 2012 Importance of hierarchical structures in wetting stability on submersed superhydrophobic surfaces. *Langmuir* **28**, 9440–9450. (doi:10.1021/la300331e)
42. Wier KA, McCarthy TJ. 2006 Condensation on ultrahydrophobic surfaces and its effect on droplet mobility: ultrahydrophobic surfaces are not always water repellant. *Langmuir* **22**, 2433–2436. (doi:10.1021/la0525877)